

Non-invasive estimation of moisture content in tuff bricks by GPR

Agliata, Rosa; Bogaard, Thom A.; Greco, Roberto; Mollo, Luigi; Slob, Evert C.; Steele-Dunne, Susan C.

DOI

[10.1016/j.conbuildmat.2017.11.103](https://doi.org/10.1016/j.conbuildmat.2017.11.103)

Publication date

2018

Document Version

Accepted author manuscript

Published in

Construction and Building Materials

Citation (APA)

Agliata, R., Bogaard, T. A., Greco, R., Mollo, L., Slob, E. C., & Steele-Dunne, S. C. (2018). Non-invasive estimation of moisture content in tuff bricks by GPR. *Construction and Building Materials*, 160, 698-706. <https://doi.org/10.1016/j.conbuildmat.2017.11.103>

Important note

To cite this publication, please use the final published version (if applicable). Please check the document version above.

Copyright

Other than for strictly personal use, it is not permitted to download, forward or distribute the text or part of it, without the consent of the author(s) and/or copyright holder(s), unless the work is under an open content license such as Creative Commons.

Takedown policy

Please contact us and provide details if you believe this document breaches copyrights. We will remove access to the work immediately and investigate your claim.

1 Non-invasive estimation of moisture content in tuff bricks by GPR

2 Rosa Agliata^{a*}, Thom A. Bogaard^b, Roberto Greco^a, Luigi Mollo^a, Evert C. Slob^c, Susan C. Steele-Dunne^b

3 ^a *Università della Campania "L. Vanvitelli", Dpt di Ingegneria Civile Design Edilizia e Ambiente, via Roma 9, 81031, Aversa (CE), Italy*

4 ^b *Delft University of Technology, Dpt of Water Management, PO-box 5048, 2600GA Delft, The Netherlands*

5 ^c *Delft University of Technology, Dpt of Geoscience and Engineering, PO-box 5048, 2600GA Delft, The Netherlands*

6 * *corresponding author, email: rosa.agliata@unicampania.it*

7 Abstract

8 Measuring water content in buildings of historical value requires non-invasive techniques to avoid the
9 damage that sample taking or probe insertion may cause to the investigated walls. With this aim, a stepped
10 frequency ground penetrating radar (GPR) system was tested to assess its applicability in moisture
11 measurements of porous masonry elements. The technique was tested on a real scale wall made with yellow
12 Neapolitan tuff bricks, a material commonly found in historical buildings of Campania (Southern Italy). First,
13 the antenna was calibrated to find its characteristic transfer functions. Then 64 GPR acquisitions, coupled
14 with gravimetric measurements of the volumetric water content, were performed on the tuff wall in
15 laboratory controlled conditions. A full inverse modelling of the GPR signal on tuff was used to retrieve
16 dielectric permittivity and electrical conductivity of tuff at various water contents. By linking these
17 characteristic electromagnetic parameters to the water content, the calibration relationships specific for
18 yellow Neapolitan tuff are defined, which can be used for moisture measurements by GPR in real case
19 studies. The experimental results lead to a robust identification of clearly defined monotonic relationships
20 for dielectric permittivity and electrical conductivity. These are characterized by high values of the
21 correlation coefficient, indicating that both parameters are potentially good proxies for water content of
22 tuff. The results indicate that GPR represents a promising indirect technique for reliable measurements of
23 water content in tuff walls and, potentially, in other porous building materials.

24 **Keywords:** moisture, non-invasive measurement, tuff masonry, ground penetrating radar, inverse modelling

25 1. Introduction

26 Measuring the water content of building materials is essential to prevent the damage that moisture may
27 cause to construction elements such as walls, but also to the plaster that protects them and even to frescoes

28 covering it. The moisture content and its distribution in a building should be repeatedly evaluated in the
29 easiest and least-invasive way possible. Based on such monitoring results, more effective decisions for
30 renovation or restoration can be made.

31 Volcanic tuff is among the building materials that show the highest ability to absorb and retain water [1,2]. It
32 is a natural pyroclastic stone, which is widespread in Campania (Southern Italy), where it has been used for
33 centuries to build vertical barriers of any kind of construction, including heritage buildings. Common
34 destructive or invasive methods cannot be used in buildings of historical value for measuring moisture
35 content, because the walls of those structures are often covered by frescos or valuable plasters. Hence,
36 novel approaches are needed to estimate the water content in porous building materials in a non-invasive
37 way. Over the years, many different techniques have been tested, such as gamma ray attenuation [3,4],
38 infrared thermography [5,6], neutron radiography [7], capacitance methods [8], non-invasive time domain
39 reflectometry [9,10,11], x-ray radiography [12,13], impedance tomography [14], evanescent-field
40 dielectrometry [15], high-frequency sensors [16], wireless inductive-capacitive sensors [17], and, recently,
41 early stage optic fibre sensors prototypes [18]. The dependence of bulk relative dielectric permittivity (ϵ_r)
42 and bulk electrical conductivity (σ) of porous media on their water content is indeed well known [19] and
43 most of the above mentioned techniques rely on that.

44 Another experimental technique sensitive to electric properties of materials and used to map the shallow
45 subsurface with high resolution is ground penetrating radar (GPR). It operates through electromagnetic
46 radiation in the microwave band of the radio spectrum, with frequencies typically comprised between a few
47 MHz and 5 GHz [20]. The transmitting antenna of the GPR system generates a signal, which propagates
48 through the material with a speed related to the dielectric permittivity of the medium, assuming the
49 magnetic permeability is that of free space. The reflected signal from the subsurface is detected by the
50 receiving antenna [21]. Thanks to its safe, rapid, non-destructive and non-invasive features, GPR continues to
51 find more civil engineering applications [22]. GPR is an established method to assess the presence of cracks
52 in road and highway pavements [23], bridges [24] and tunnels, and to perform in-situ quality control of
53 density and moisture content of fresh bituminous mixtures [25,26]. In addition, the GPR method is widely

54 used in geological surveys to detect subsurface cavities and voids [27], map soil layers and texture [28], and
55 to image the foundations of buildings and their surroundings [29]. Another successful application of GPR is
56 the discovery of buried archaeological objects [30] and underground utilities such as gas and water pipes
57 [31]. GPR can also be used to evaluate the electromagnetic properties [32,33] and moisture content of soils
58 [34,35,36].

59 In the building industry, subsurface remote sensing is a useful tool to detect inclusions [21], voids [37,38]
60 and damage [39,40,41] and to measure the water content [42,43,44,45,46,47,48] over a wide area of a
61 construction in a non-invasive way. It is worth noting that this analysis enables to obtain a more complete
62 picture of the state of health of a building than single-point tests (e.g. drilling) [49].

63 In this study the feasibility of using the GPR technique to measure the moisture content in yellow volcanic
64 tuff masonry without damaging the historical heritage is evaluated. The procedure to characterize the
65 response of the antenna and the forward model adopted for GPR data processing are described. Then, the
66 results of GPR experiments on a real scale wall are presented, with the aim of calibrating the GPR response
67 to water content variations. The relationships linking dielectric permittivity and electrical conductivity of
68 volcanic tuff to its volumetric water content are identified. Finally, the quality with which the water content
69 can be estimated from GPR reflection data is assessed. This initial calibration phase is indeed essential to
70 carry out GPR surveys in real case studies.

71 2. Theory of ground-penetrating radar system

72 A stepped frequency continuous wave (SFCW) radar, combined with a dielectric-filled transverse electric and
73 magnetic (TEM) linear polarized double ridged broadband horn antenna (BBHA 9120 A, Schwarzbeck - Mess-
74 Elektronik) used off-ground in monostatic mode (i.e. a single antenna used as emitter and receiver) was used
75 to map the dielectric permittivity and electrical conductivity of the subsurface. This radar configuration
76 allows an effective and realistic modelling of the radar-antenna-subsurface system [50]. A SFCW radar
77 enables the user to control an ultra-wide frequency band (UWB) that results in a finer depth resolution.
78 Moreover, for this type of radar, the effect of the dispersive properties of the UWB antennas on the
79 measurements can be taken into account by performing a prior calibration. Performing measurements with

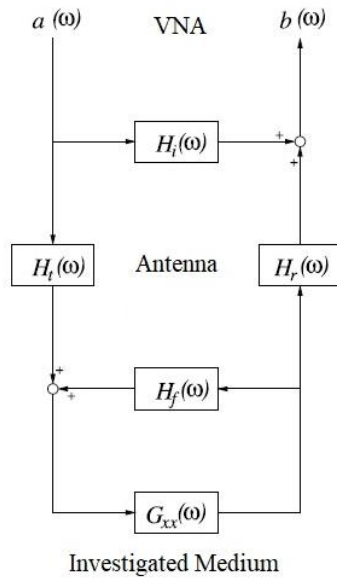
80 an SFCW radar has two more advantages over those with a pulse radar. Firstly, pulse radars are subsampled
81 and require many emissions to build a measurement in the time window of interest, whereas at each
82 frequency an independent measurement is taken. Secondly, at each frequency the same signal strength can
83 be achieved, whereas for pulse radars most of the energy is concentrated around a so-called centre
84 frequency. A ZVH8 Cable and Antenna Analyzer (ZVH8, 100 kHz to 8GHz, Rohde & Schwarz, München,
85 Germany) with the K42 Vector Network Analyzer and K40 Remote Control options was used to emulate an
86 UWB-SFCW radar system. The antenna is 195 mm long, has an aperture of 245 x 142 mm², and operates in
87 the range of 0.8 – 5 GHz. It was connected to Port 1 of the VNA via an N-type 50 Ohm coaxial cable. This
88 setup allows for a measured GPR signal consisting of the complex ratio $S_{11}(\omega)$ between the reflected signal
89 and the emitted signal, ω being the angular frequency [51].

90 The VNA was calibrated at the connection between its feed point and the cable using the *Open*, *Short* and
91 *Match* loads of a high precision standard calibration kit (85032B Type-N, 50 Ohm, Keysight Technologies).
92 This procedure is necessary to establish a reference plane where S_{11} is measured. The radar-antenna-
93 subsurface system was modelled using the block diagram shown in Fig.1, as introduced by Lambot et al. [32].
94 The proposed model for describing the radar signal is based on two main assumptions. First, the shape of the
95 electromagnetic field received by the antenna is independent of the target, meaning that only the phase and
96 amplitude of the field are functions of the target. This assumption has been proven to be valid when the
97 investigated surface is situated in the far-field region of the antenna [32,33], which can then be modelled
98 accurately as an interactive point source and point receiver rather than as a spatially distributed source and
99 receiver. Second, the subsurface can be described as a horizontally layered medium [51], which is a
100 consequence of the first assumption, provided that any horizontal variability of the electric properties of the
101 investigated medium is neglected.

102 The measured signal can be given in terms of the earth's impulse reflection response and the antenna
103 transfer functions, expressed in the frequency domain as

$$104 \quad S_{11}(\omega) = \frac{b(\omega)}{a(\omega)} = H_i(\omega) + \frac{H(\omega)G_{xx}(\omega)}{1-H_f(\omega)G_{xx}(\omega)} \quad (1)$$

105 where $b(\omega)$ and $a(\omega)$ are received and emitted signals at the VNA reference plane, respectively. $H_i(\omega)$ is
 106 the return loss, $H(\omega) = H_t(\omega)H_r(\omega)$ is the transmitting-receiving transfer function, $H_f(\omega)$ is the feedback
 107 loss, and $G_{xx}(\omega)$ is the earth's impulse reflection response, also known as the scattered Green's function
 108 [52,53,54] of the air-subsurface system, modelled as a layered medium. For this model configuration, the
 109 approach given in Slob and Fokkema [55] and Lambot et al. [51] is used to determine $G_{xx}(\omega)$ (that is the the
 110 exact solution of the 3-D Maxwell's equations for wave propagation in a horizontally multilayered medium)
 111 by computing recursively the transverse electric and magnetic global reflection coefficients of the
 112 multilayered system in the two-dimensional spatial Fourier domain.

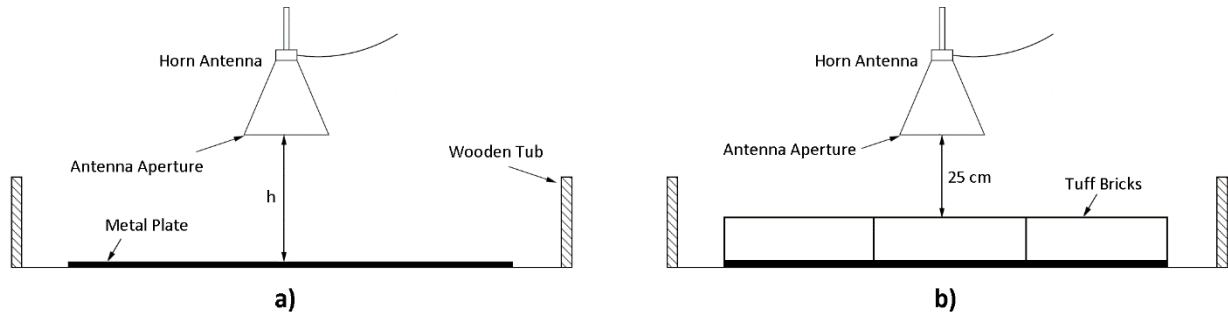


113
 114 **Fig. 1** Block diagram representing the radar-antenna-subsurface system, modelled as linear systems in series and parallel, where $a(\omega)$
 115 and $b(\omega)$ are the emitted and received waves at the VNA reference plane, respectively; $H_i(\omega)$ is the return loss; $H_t(\omega)$ and $H_r(\omega)$ are
 116 the transmitting and receiving transfer functions, respectively; $H_f(\omega)$ is the feedback loss; and $G_{xx}(\omega)$ is the transfer Green's function
 117 of the air-subsurface system (redrawn after [50]).

118
 119 **2.1 Calibration of the antenna**

120 In the adopted setup, a metal plate was placed centrally below the antenna, as shown in Fig. 2a. It is large
 121 enough to be modelled as an infinite perfect electric conductor. The antenna transfer functions $H_i(\omega)$, $H(\omega)$
 122 and $H_f(\omega)$, can be obtained by solving equation (1) for different distances between the metal plate and the
 123 antenna aperture. More than 3 different configurations should be used to overcome possible problems with
 124 numerical instability of the solution at some frequencies [50]. Here 11 different distances were used, ranging
 125 between 25 cm and 35 cm (25, 25.8, 26.6, 27.6, 28.6, 29.7, 30.6, 31.6, 32.5, 33.6 and 34.8 cm). The

126 anticipated experiments should be taken somewhere inside this range and the range is the interval where
 127 the assumptions are deemed valid.
 128 For each height, the $S_{11}(\omega)$ functions can be measured and the Green's functions $G_{xx}(\omega)$ can be computed.
 129 The unknown transfer functions are then found from the measured S_{11} by minimizing equation (1) in the
 130 least squares sense using all distances.



131
 132 **Fig. 2** Sketches of the experimental setup adopted for the calibration of the antenna (a) and for the determination of the
 133 relationships linking dielectric permittivity and electrical conductivity of tuff with its volumetric water content (b).

134 2.2 Tuff bricks electric properties

135 The constitutive parameters governing electromagnetic wave propagation are dielectric permittivity ϵ
 136 (Fm^{-1}), electrical conductivity σ (Sm^{-1}), and magnetic permeability μ (Hm^{-1}). The latter can be assumed equal
 137 to the permeability of free space ($\mu_0 = 4\pi \times 10^{-7} \text{Hm}^{-1}$), which is valid for non-magnetic materials, as in the
 138 present case. The relative dielectric permittivity is defined as $\epsilon_r = \epsilon/\epsilon_0$, where $\epsilon_0 = 1/(\mu_0 c_0^2)$ is the permittivity
 139 of free space ($c_0 = 2.998 \times 10^8 \text{ms}^{-1}$ being the speed of electromagnetic waves in vacuum).

140 The relative dielectric permittivity is considered independent of the frequency while the electrical
 141 conductivity can depend on frequency as a consequence of relaxation mechanisms as well as the Maxwell-
 142 Wagner effect [56,57,58,59,33]. To determine if σ is frequency dependent, it was first considered
 143 independent and then linearly dependent on frequency as described by:

$$144 \quad \sigma(f) = \sigma_{1\text{GHz}} + a (f - 10^9) \quad (2)$$

145 where f is the frequency, $\sigma_{1\text{GHz}}$ is the reference electrical conductivity at 1 GHz, and a is the slope of $\sigma(f)$. The
 146 electrical conductivity of sandy soils can be well estimated by equation (2) when the frequency ranges from
 147 1 to 3 GHz. For this reason 3 GHz is taken as the upper limit (f_{max}) of the experiment, as the electrical
 148 conductivity of tuff is assumed to be similar to that of sand ($0.01 - 1 \text{Sm}^{-1}$). 0.8 GHz was chosen as the lower

149 limit (f_{min}), which is the minimum operational frequency of the antenna. The attenuation of the wave
 150 amplitude along the two-way travel path through the tuff bricks (i.e. 21 cm) was such that the reflected
 151 signal was clearly detectable across the entire range of frequency, thus allowing a reliable estimate of the
 152 electric properties of the investigated medium. In fact, the worst condition occurs at f_{max} near saturation
 153 conditions, when the high values of electrical conductivity and permittivity cause the biggest attenuation.
 154 Being the skin depth (s_d) the distance at which the wave amplitude decreases to $1/e^2$ of the emitted value,
 155 this distance can be calculated by [60]:

$$156 \quad s_d = \frac{c}{2\pi f \sqrt{\frac{\epsilon_r}{2} \left[\sqrt{1 + \left(\frac{\sigma}{2\pi f \epsilon_0} \right)^2} - 1 \right]}} \quad (3)$$

157 In the worst condition, brick thickness is about $1.36 * s_d$, indicating full penetration of the signal.
 158 In the considered interval, S_{11} was acquired sequentially at 1201 stepped operating frequencies with a
 159 frequency step of around 1.8 MHz.

160 2.3 Modelling of the Radar Signal: Model Inversion

161 Subsurface parameter identification was formulated as an inverse problem in the least squares sense and an
 162 objective function to be minimized, expressing the amplitude of the model errors as a Normalized Root
 163 Mean Square Error (NRMSE), was defined as follows [40]:

$$164 \quad \varphi(\mathbf{b}) = \left(\frac{\sum_{f_{min}}^{f_{max}} |G_{xx}^{obs} - G_{xx}^{pre}|^2}{\sum_{f_{min}}^{f_{max}} |G_{xx}^{obs}|^2} \right)^{1/2} \quad (4)$$

165 where $\mathbf{G}_{xx}^{obs} = G_{xx}^{obs}(\omega)$ and $\mathbf{G}_{xx}^{pre} = G_{xx}^{pre}(\omega, \mathbf{b})$ are the complex vectors containing the observed and the
 166 predicted Green's functions, respectively. The parameter vector \mathbf{b} contains the unknowns and is given by
 167 $\mathbf{b} = [\epsilon_r, \sigma]$ (or $\mathbf{b} = [\epsilon_r, \sigma_{1GHz}, a]$ when σ is considered as frequency dependent).

168 To find estimates for the unknowns, the objective function $\varphi(\mathbf{b})$ should be minimized. This minimization
 169 problem is ill-posed and non-unique, and the objective function may present many local minima. Usually,
 170 this problem is solved by iterative forward modelling with the aim to minimize the number of iterations
 171 necessary to find the best estimate for the unknown parameters. In this case, given the limited number of

172 parameters to be identified, a full solution space can be explored with a metaheuristic variable
173 neighbourhood search method [61]. A large parameter space ($1 < \epsilon_r < 20$; $1 \times 10^{-3} < \sigma_{1\text{GHz}} < 1 \times 10^{-1} \text{ Sm}^{-1}$; $1 \times 10^{-12} < a < 1 \times 10^{-10} \text{ Ssm}^{-1}$) was investigated to avoid local minima of the objective function. This is initially done
174 with relatively large steps, such that subsequent investigations are performed in a smaller region of the
175 parameter space around the provisional local minimum until the best estimate is found, representing the
176 solution of the inverse problem.

178 3. Materials and methods

179 3.1 Experimental Setup and procedure

180 For the test, 15 bricks of yellow volcanic tuff (porosity = 50% [2,62]) were acquired from a surface quarry in
181 Quarto, near Naples, southern Italy. The average dimensions of each tuff brick are 10 x 24 x 38 cm (average
182 volume 9.2 dm^3). The dry bulk density of the bricks (γ) was calculated by measuring the mass and volume of
183 6 of the bricks and averaging the obtained values. The soaking ratio was experimentally determined as the
184 ratio between the mass of water absorbed at saturation by one brick and its oven-dried mass.

185 The bricks were arranged in the form of a horizontal wall, with one of the two major surfaces lying on the
186 ground (Fig. 2b). This arrangement prevented the formation of horizontal moisture gradients within the
187 experimentally investigated area, as required by the second assumption stated in section 2.1. To avoid
188 distortions due to air gaps, quick-setting cement was used to assemble the stones together to fill the fissures
189 at the interface of bricks (see subsection 2.2.1).

190 The assembled wall, measuring approximately 123 x 110 cm, was built in a tub with wooden frames (inner
191 dimensions 190 x 160 cm), in an indoor environment under controlled temperature (18-20° C) and relative
192 humidity ($\text{RH} \approx 0.7$). The tub was made impervious by covering the inner surface with a double layer of strong
193 plastic sheet. Below the plastic sheet, a horizontal metal plate was installed to control the bottom boundary
194 conditions in the electromagnetic model, so that materials placed underneath the metal plate had no
195 influence on the measured backscattered signal. The antenna was located 25 cm above the surface of the
196 tuff bricks, with a footprint (at this height and for the considered frequency interval) of around 80 x 80 cm.

197 Ten microwave absorbing foam panels, with the dimensions of 70 x 70 cm, were placed around the tub to
198 prevent the measurements being influenced by the presence of metal objects around the setup that could
199 cause spurious reflections in the backscattered signal.

200 A prism-shaped sample (14 x 24 x 9.5 cm), used as a reference, was obtained by cutting off one half from
201 one of the 15 bricks, and coated on the side surfaces with waterproofing spray to mimic the moisture
202 conditions of the bricks located in the middle of the wall. The sample stone was placed in the tub beside the
203 tested wall and served as gravimetric reference to retrieve the amount of water contained in the bricks, by
204 weighing it using an electronic balance (FKB by KERN & SOHN GmbH) with an accuracy of 0.1 g.

205 The experimental setup is shown in Fig. 3. Before wetting the wall, a GPR response was acquired and the
206 weight of the sample stone measured. Then, the wall and the sample stone were submerged for 42 hours.
207 When saturation was achieved, water was removed from the tub with a pump, and the drying phase started.
208 During this phase, the sample stone was weighed at different time intervals for 15 days. Simultaneously, the
209 GPR waveforms were acquired every 5 minutes in the beginning of the experiment, and increasing up to 15
210 minutes when reaching the end of the experiment. A total of 64 coupled acquisitions were made.

211 When the experiment ended, the sample was subjected to a drying stage in a stove at 105°C for 48 h. The
212 weight of the oven-dried sample stone was used as a reference to calculate the volumetric water content of
213 the sample stone at each gravimetric measurement [63].



214

215

Fig. 3 View of the experimental setup

216 3.2 Surface Roughness Characterization

217 Surface roughness can be considered as a major source of noise in subsurface mapping [64]. If the top
218 surface is smooth, then the back reflected signal would be mostly consisting of specular reflection, meaning
219 that the incident and the reflected rays would have the same angle of incidence. On the other hand, if the
220 surface is rough, then diffuse reflection might occur. Indeed, the incident ray reaching the surface of the
221 medium, would be split and reflected back at many angles rather than one, by localized irregularities of the
222 surface, causing distortion of electromagnetic signals. This effect, also known as scattering, needs to be
223 taken into account in signal processing (e.g. [65,50]).

224 The most commonly used criterion to define a surface as smooth or rough, from an electromagnetic point of
225 view, is Rayleigh's criterion (e.g. Boithias [66]). For a monostatic mode of operation (adopted in this study), a
226 surface is considered rough if the average height of the surface protrusions is bigger than the critical height
227 ($h_m \geq h_c$). The critical height could be described as function of the wavelength (λ)

$$228 \quad h_c = \lambda/8 \quad (5)$$

229 with $\lambda = c_0/f$.

230 Alternatively, the surface roughness of the tuff bricks was measured by a Terrestrial Laser Scanning (TLS)
231 survey, using a Leica C10 laser scanner, with the tuff bricks juxtaposed next to each other, over an area of 75
232 x 75 cm², contained in the antenna footprint.

233 4. Results and Discussion

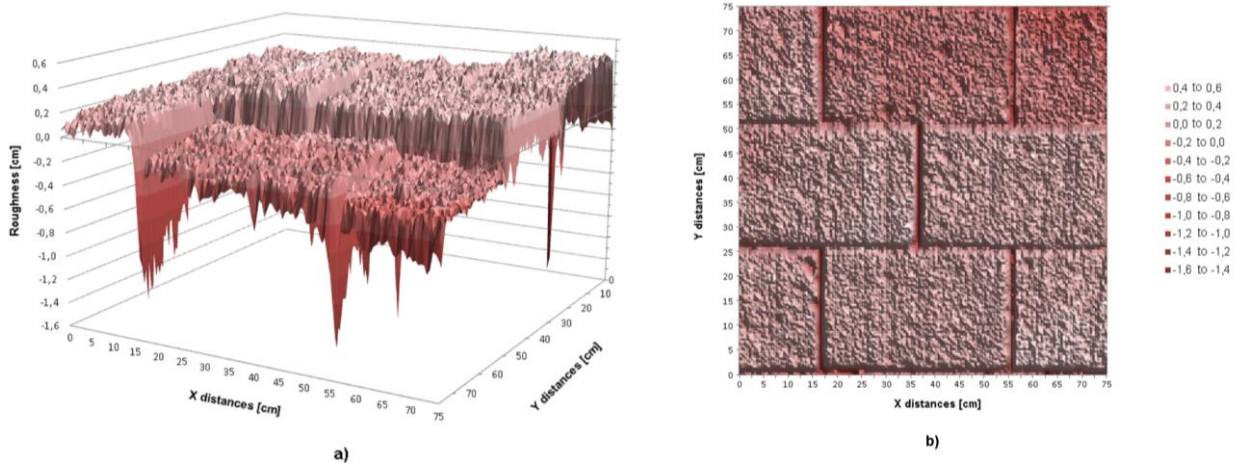
234 4.1 Characterization of the bricks

235 The calculated dry bulk density and the soaking ratio of the bricks were 1.33 kg/dm³ and 24%, respectively.

236 These values are consistent with the typical literature values for yellow Neapolitan tuff [2,53].

237 Regarding the surface roughness characterization, the critical height (h_c) of the protuberances calculated,
238 according to equation (5), for the lowest (0.8 GHz) and the highest (3 GHz) used frequencies were 4.70 cm
239 and 1.25 cm, respectively. The results of the laser scan test, shown in Fig. 4, highlighted that the maximum
240 height of the surface protuberances (h_{max}) was smaller than 0.6 cm, which is perfectly compatible with the
241 GPR requirements ($h_{max} < h_c$). Conversely, the dimension of the fissures between the bricks (reaching 1.5 cm)

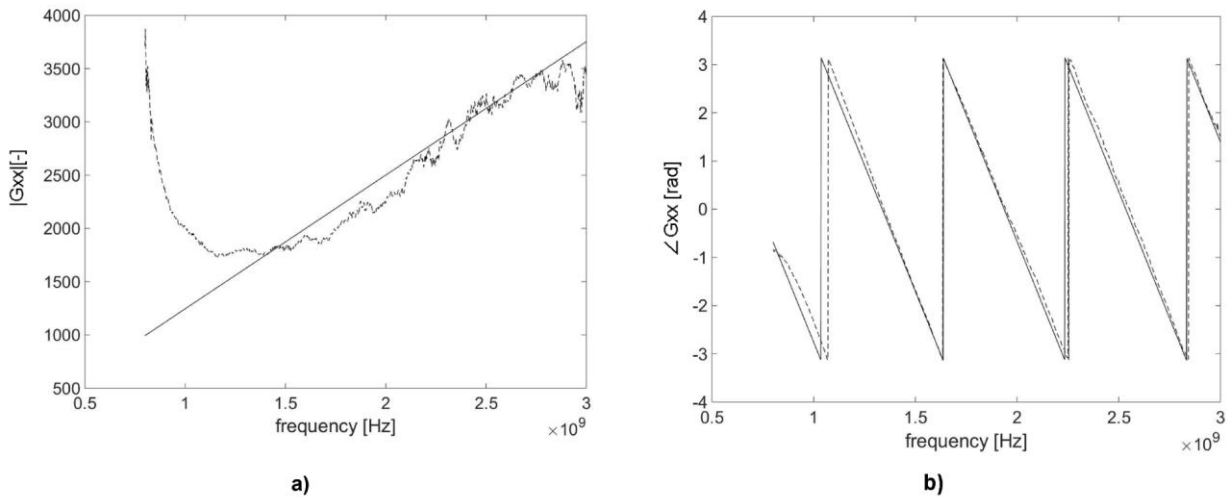
242 exceeded the critical height at high frequencies, so it could affect the measurements. For this reason, the
 243 gaps were all sealed with a cement admixture before starting the acquisitions with GPR, as explained in
 244 section 2.2.



245
 246 **Fig. 4** Characterization of the surface roughness recorded by the laser scanner in 3D view (a) and intensity colour map (b)

247 **4.2 Characterization of the Antenna**

248 As explained in section 2.1.1, the characterization of the antenna consists of a series of measurements to
 249 determine the antenna transfer functions.



250
 251 **Fig. 5** Observed (dashed line) and predicted (solid line) Green's function in air (antenna characterization phase) at 25 cm distance
 252 from the metal plate: amplitude vs. frequency (a); phase angle vs. frequency (b)

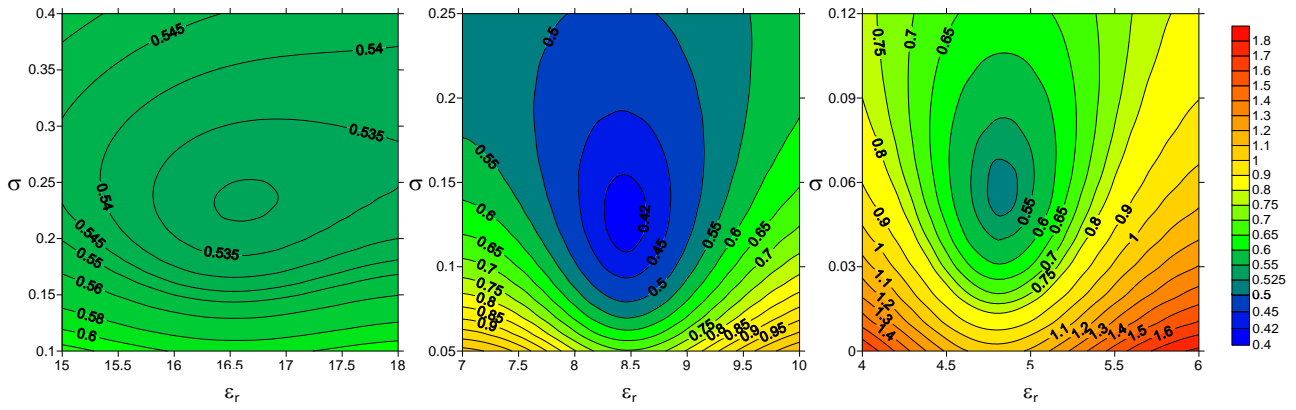
253 As an example, Fig. 5 shows the observed and predicted Green's response functions during the
 254 characterization of the antenna, when the latter was suspended at 25 cm distance from the metal plate. This
 255 fixed distance was also adopted during the entire experiment on tuff. It can be observed from Fig. 5 that the

256 phase (Fig. 5b) is better reproduced than the amplitude (Fig. 5a). The predicted Green's function amplitudes
257 show a global NRMSE of 0.252. However, considering only the range 1.2 – 3 GHz, the calculated NRMSE
258 decreases to 0.158. The agreement between observed and predicted phase shown in Fig. 5b is satisfactory
259 over the entire investigated frequency interval. In view of the error values, the experimental results are
260 analysed only within the 1.2 – 3 GHz frequency range.

261 4.3 Characterization of GPR response of tuff

262 As indicated in section 2.1.2, for the modelling of the Green's functions simulating the response of GPR on
263 tuff, two alternative assumptions were made: a) no dependence of the electrical conductivity on frequency;
264 b) electrical conductivity linearly dependent on frequency, according to equation (2). The results obtained
265 indicate that, for the considered frequency interval, the use of equation (2) does not lead to a significant
266 improvement of the ability of the model to reproduce the observed Green's function. The objective function
267 ϕ , ranging between 0.346 and 0.536 in both cases, reveals a slight improvement only in few cases, with the
268 maximum improvement of 0.04 achieved in the driest tested conditions. Furthermore, the introduction of an
269 additional parameter to be identified with the inverse modelling (namely, the two parameters $\sigma_{1\text{GHz}}$ and a of
270 equation (2) in place of the constant σ), results in a more complex inverse problem and did not improve the
271 identification of the searched characteristic relationships $\theta(\epsilon_r)$ and $\theta(\sigma)$ holding for tuff. Concerning the
272 inversely estimated relationship $\theta(\epsilon_r)$, there is almost no difference whether the electrical conductivity is
273 considered dependent on frequency or not. Therefore, the identified ϵ_r values are nearly the same and the
274 two curves, describing the best-fitting calibration relationships $\theta(\epsilon_r)$, perfectly overlay. Conversely, when the
275 electrical conductivity is considered dependent on frequency, it is no longer possible to establish a $\theta(\sigma)$
276 relationship, unless we consider the value of σ at 1GHz. The obtained $(\theta, \sigma_{1\text{GHz}})$ points, however, do not show
277 a physically sound monotonic pattern, leading to an ill-defined $\theta(\sigma_{1\text{GHz}})$ relationship. For all these reasons,
278 the results presented hereafter assume that σ is independent of frequency.

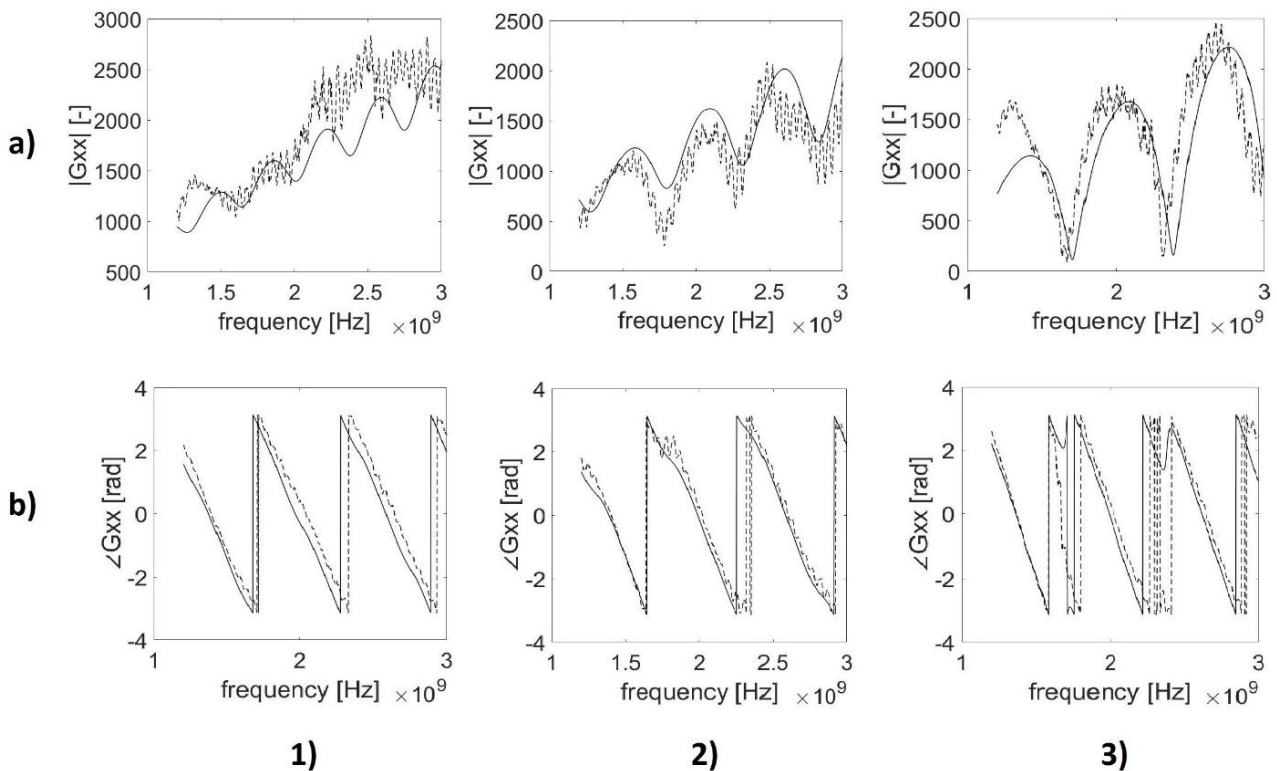
279 The minimum values of the objective function ϕ of equation (4), obtained for the 64 coupled acquisitions,
280 indicate that the propagation of the electromagnetic field through the partially saturated tuff wall was
281 difficult to interpret under the simplifying assumptions introduced in the model.



282

283 **Fig. 6** Contour plots of the objective function ϕ vs. ϵ_r and σ for three different water contents: maximum saturation (a); end of the
 284 drying phase (b); steady conditions (c).

285 Three examples of the contour plots of the objective function $\phi(\epsilon_r, \sigma)$ are shown in Fig. 6 for three different
 286 moisture contents of the tuff: maximum degree of saturation, recorded just after the wetting phase (Fig. 6a);
 287 end of the drying phase (Fig. 6b); steady conditions recorded at the beginning of the experiment and
 288 representing the driest measured condition (Fig. 6c). The corresponding values of the objective function are
 289 0.531, 0.410 and 0.516, respectively. In all cases, and especially for the two driest conditions, a marked
 290 minimum of the objective function in the investigated region of the parameter space is clearly visible,
 291 indicating a good sensitivity of the GPR response to the variations of dielectric properties related to water
 292 content of tuff.

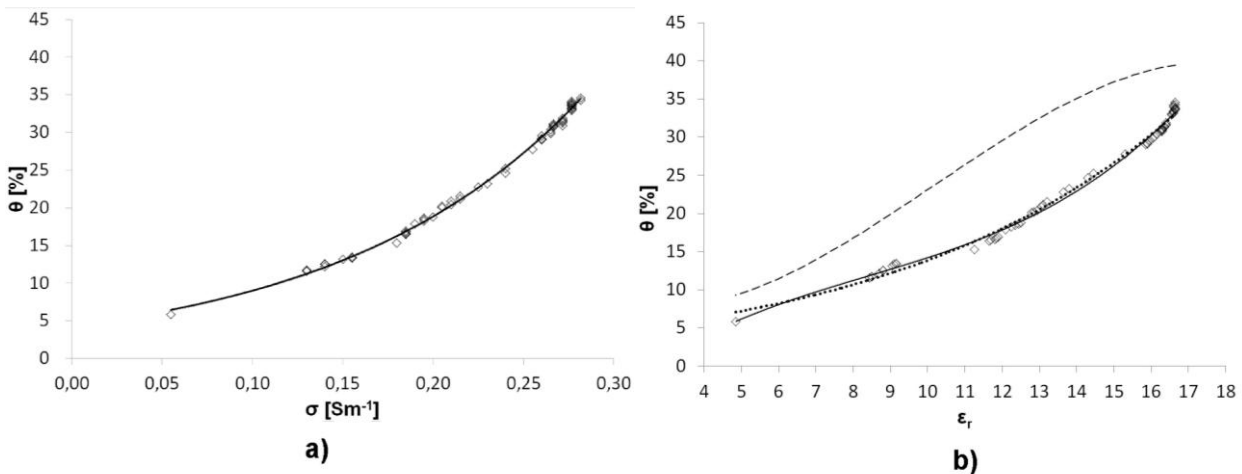


293

294 **Fig. 7** Amplitude (a) and phase (b) of Green's functions of tuff (with σ constant with frequency) for three different water contents:
 295 maximum saturation (1); end of the drying phase (2); steady conditions (3). The dashed and the solid lines represent the observed and the predicted G_{xx} respectively.
 296

297 Fig. 7 represents the observed and predicted G_{xx} in frequency domain for the same three different moisture
 298 contents. The phase angle is fairly well described in all the situations, while the amplitude improves with
 299 decreasing water content. Two different types of errors may affect the modelling of the amplitude of the
 300 Green's function: local disturbance and overall trend. As already stated by Lambot et al. [32], the punctual
 301 clutter can be ascribed to the approximation of the metal plate, used for the calibration of the antenna, to
 302 an infinite perfect conductor, as well as to the presence of extraneous sources of scattering (e.g. metallic
 303 objects) in the laboratory. Conversely, the reason of the general discrepancy between the observed and
 304 predicted Green's function amplitudes is harder to identify, as it lies in the hypotheses described in section
 305 2.1 and used to build the model. It is worth noting that also the finite size of the experimental setup and the
 306 unrelated scatterers around it may lead to the observed mismatch [32,51].

307 The plots of the amplitude of G_{xx} (Fig. 7, a1 to a3) confirm that the effect of the frequency dependence of
 308 the electrical conductivity, that should result in a decrease in the amplitude of the Green's function with
 309 increasing frequency [40], was not very important in the analysed conditions.



310 **Fig. 8** Experimental points and best-fitting calibration relationships for tuff (eqq. 6, 7 and 8). Panel (a) shows the relationship linking
 311 electrical conductivity σ with volumetric water content θ . In panel (b) the identified relationships between relative dielectric
 312 permittivity ϵ_r and θ (solid line for the polynomial and dotted line for the exponential) are compared with the analogous
 313 relationship (dashed line) retrieved in our previous research by means of Time Domain Reflectometry [67].
 314

315 Fig. 8 represents the volumetric water content as a function of the inversely estimated electrical conductivity
 316 (Fig. 8a) and relative dielectric permittivity (Fig. 8b). The tuff-specific best-fitting empirical model was

317 retrieved by minimizing the NRMSE of the 64 coupled measurements. The relationship $\theta(\sigma)$ is well described
318 ($R^2 = 0.997$) by the exponential curve given by:

319
$$\theta(\sigma) = 4,3036e^{7.3891\sigma} \quad (6)$$

320 The relationship between the dielectric permittivity and the water content, $\theta(\epsilon_r)$, can be described by an
321 exponential curve (equation 7) and by a third order polynomial (equation 8) similar to Topp's equation for
322 unsaturated soils [67]

323
$$\theta(\epsilon_r) = 3.7615e^{0.1305\epsilon_r} \quad (7)$$

324
$$\theta(\epsilon_r) = 0.0169\epsilon_r^3 - 0.4262\epsilon_r^2 + 5.0446\epsilon_r - 10.4974 \quad (8)$$

325 Although the exponential curve slightly overestimates the water content in dry conditions, the closeness of
326 R^2 to 1 for both the retrieved relationships ($R^2 = 0.989$ and $R^2 = 0.995$, respectively), indicates a good fit of
327 the obtained curves to the experimental results over the entire investigated water content range.

328 The obtained calibration curves show that both electrical conductivity and dielectric permittivity measured
329 by means of GPR are a good proxy for volumetric water content of tuff. However, as the bulk electrical
330 conductivity of tuff depends on the electrical conductivity of pore water, and hence on the dissolved ions
331 concentration, the $\theta(\epsilon_r)$ relationship appears more suitable for general use in real masonry elements.

332 Further research is needed to extend the obtained results towards real applications. The capability of GPR to
333 estimate water content in vertical walls, where heterogeneous water content distribution is likely expected,
334 should be tested. A possible solution to overcome this problem could be using a smaller footprint, e.g.
335 achievable with an antenna of smaller dimensions, compatibly with the thickness of the investigated wall.

336 5. Conclusions

337 This study investigates the feasibility of using a stepped frequency GPR system to measure the volumetric
338 water content of tuff bricks. The adopted full search of the solution space to model the measured GPR data
339 allows obtaining the best estimate of permittivity and conductivity.

340 Measurements were carried out on a real scale tuff wall by coupling GPR signal full wave inverse modelling
341 with gravimetric measurements of tuff brick water content, in the range 0.05 to 0.35. Then, specific

342 calibration curves were obtained by linking the retrieved dielectric permittivity and electrical conductivity to
343 the measured water content of tuff.

344 The dielectric permittivity of tuff is assumed independent of frequency within the interval considered (1.2
345 GHz to 3 GHz) and the results obtained indicate that the electrical conductivity can be considered
346 independent of frequency as well.

347 Important errors affect the mathematical reconstruction of the GPR experimental signals. However, in all
348 cases a clear, unique minimum of the objective function can be found in the investigated region of the
349 parameter space investigated. The occurrence of this minimum indicates an unambiguous link between the
350 dielectric permittivity and electrical conductivity of tuff and its water content.

351 The experimental results lead to a robust identification of clearly defined monotonic relationships for both
352 dielectric permittivity and electrical conductivity. High correlation values indicate that dielectric permittivity
353 and electrical conductivity are potentially good proxies to determine water content of tuff bricks. Because
354 bulk electrical conductivity strongly depends on the electrical conductivity of the pore water, the relationship
355 linking the dielectric permittivity and water content is preferred in real case studies.

356 GPR represents a promising indirect technique for reliable measurements of water content in tuff walls.
357 Furthermore, because it is completely non-invasive, it may be considered a potentially suitable method for
358 quantitative monitoring of moisture content of masonry elements in heritage buildings.

359 Further research will focus on the estimation of the water content in a real wall, extending the proposed
360 model to more complex configurations (e.g. in presence of a plaster layer).

361 **Acknowledgments**

362 This research is part of the Ph.D. project "*Non-invasive moisture measurements in porous building materials*"
363 within the Doctoral Course "A.D.I." of Università degli studi della Campania 'L. Vanvitelli', supported by
364 Campania Region through the P.O.R. Campania FSE 2007-2013, D.D. n. 25, 18/02/2014.

365 We thank dr. Belen Riveiro for assistance with Laser Scan survey, eng. Fred van der Zwan for support and
366 providing materials for the experimental setup, and eng. Sina N. Dezfuli for providing language help and
367 suggestions that improved the manuscript. We also thank the Faculty of Civil Engineering and Geoscience of
368 Technical University of Delft, which hosted all the experiments at Waterlab.

369

370

371 **References**

- 372 1. R. Brown, Geology and the conservation of antique monuments in Turkey. *Environ. Geol. Water Sci.*
373 9.2(1987) 71–84.
- 374 2. A. Colella, D. Calcaterra, P. Cappelletti, C. Di Benedetto, A. Langella, L. Papa, A. Perrotta, C. Scarpati, M.
375 De Gennaro, Il Tufo Giallo Napoletano, in: M. De Gennaro, D. Calcaterra, A. Langella (Eds.), *Le Pietre*
376 *Storiche della Campania dall’oblio alla riscoperta*, Luciano Editore, Napoli, Italy, 2013, pp. 129–154.
- 377 3. A.F. Nielsen, Gamma-ray attenuation used for measuring the moisture content and homogeneity of
378 porous concrete. *Build. Sci.* 7(1972) 257–263.
- 379 4. M.K. Kumaran, M.T. Bomberg, A gamma-spectrometer for determination of density distribution and
380 moisture distribution in building materials, National Research Council Canada, Division of Building
381 Research, 1985.
- 382 5. A. Marshall, Detecting Moisture in Buildings Using Infrared Thermography, in: *Thermal Infrared Sensing*
383 *Applied to Energy Conservation in Building Envelopes: Thermosense III*, International Society for Optics
384 and Photonics, 1981, pp. 111-118.
- 385 6. A. Tavukcuoglu, A. Duzgunes, E.N. Caner-Saltik, S. Demirci, Use of IR thermography for the assessment
386 of surface-water drainage problems in a historical building, Agzikarahan (Aksaray), Turkey, *NDT&E Int.*
387 38.5 (2005) 402-410.
- 388 7. L. Pel, A.A.J. Ketelaars, O.C.G. Adan, A.A. Van Well, Determination of moisture diffusivity in porous
389 media using scanning neutron radiography, *Int. J. Heat Mass Transfer*, 36.5(1993) 1261–1267.
390 doi:10.1016/S0017-9310(05)80095-X.
- 391 8. P. Semerák, R. Černý, A capacitance method for measuring the moisture content of building materials,
392 *Stavební obzor* 6(1997) 102-103.
- 393 9. T. Hauschild, F. Menke, Moisture measurement in masonry walls using a non-invasive reflectometer,
394 *Electronics Letters* 34.25 (1998): 2413-2414.
- 395 10. Z. Suchorab, Laboratory measurements of moisture in a model red-brick wall using the surface TDR
396 probe, *Proc., ECOpole* 7.1(2013) 171–176.
- 397 11. Z. Suchorab, Non-invasive moisture measurement in building materials, *Environmental engineering IV*,
398 Taylor & Francis Group, London, 2013, pp. 433-439..
- 399 12. K.K. Hansen, S.K. Jensen, L. Gerward, K. Singh, Dual-energy X-ray absorptiometry for the simultaneous
400 determination of density and moisture content in porous structural materials, in: *5th symposium on*
401 *building physics in the Nordic countries*, Chalmers tekniska högskola, 1999. pp. 281-288.
- 402 13. S. Roels, J. Carmeliet, Analysis of Moisture Flow in Porous Materials using Microfocus X-ray Radiography,
403 *Int. J. Heat Mass Transfer* 49.25(2006) 4762–4772.

- 404 14. P. Berowski, S.F. Filipowicz, J. Sikora, S. Wojtowicz, Dehumidification of the wall process monitoring
405 using 3D EIT system, in: 15th Conference on the Computation of Electromagnetic Fields COMPUMAG,
406 Vol. 2, Shenyang, China, 2005, pp. 166-67.
- 407 15. V. Di Tullio, N. Proietti, M. Gobino, D. Capitani, R. Olmi, S. Priori, C. Riminesi, E. Giani, Non-destructive
408 mapping of dampness and salts in degraded wall paintings in hypogeous buildings: the case of St.
409 Clement at mass fresco in St. Clement Basilica, Rome. *Anal. Bioanal. Chem.* 369(2010) 1885-1896.
- 410 16. G. Gärtner, R. Plagge, H. Sonntag, Determination of moisture content of the outer wall using hf-sensor
411 technology, gg-projekt 2010.
- 412 17. G. Stojanovic, M. Radovanovic, M. Malesev, V. Radonjanin, Monitoring of water content in building
413 materials using a wireless passive sensor, *Sensors* 10(2010) 4270–4280.
- 414 18. A. Minardo, E. Catalano, L. Zeni, R. Agliata, R. Greco, L. Mollo, Measurement of moisture content in
415 masonry materials by active distributed optical fiber sensors, in: *Photonic Technologies (Fotonica 2016)*,
416 18th Italian National Conference on, IET, 2016, pp. 1-3.
- 417 19. P. Hoekstra, A. Delaney, Dielectric properties of soils at UHF and microwave frequencies, *Journal of*
418 *Geophysical Research Solid Earth and Planets* 79.11(1974) 1699-1708. DOI: 10.1029/JB079i011p01699.
- 419 20. E. Slob, M. Sato, G. Olhoeft, Surface and borehole ground penetrating radar developments, *Geophysics*
420 75(2010) 75A103-75A120.
- 421 21. M.N. Soutsos, J.H. Bungey, S.G. Millard, M.R. Shaw, A. Patterson, Dielectric properties of concrete and
422 their influence on radar testing, *NDT&E Int.* 34.6(2001) 419-425.
- 423 22. H. Jol, *Ground penetrating radar: Theory and applications*, Elsevier, 2008.
- 424 23. D.R. Huston, N.V. Pelczarski, B. Esser, K.R. Maser, Damage detection in roadways with ground
425 penetrating radar, in: *Eighth International Conference on Ground Penetrating Radar*, International
426 Society for Optics and Photonics, 2000, pp. 91-95.
- 427 24. D. Huston, J. Hu, K. Maser, K. Weedon, C. Adam, Ground penetrating radar for concrete bridge health
428 monitoring applications, *Nondestructive Evaluation of Bridges and Highways III*, International Society for
429 Optics and Photonics, Newport Beach, CA, 1999, pp. 170-180.
- 430 25. C.P. Plati, A. Loizos, Estimation of in-situ density and moisture content in HMA pavements based on GPR
431 trace reflection amplitude using different frequencies, *J. Appl. Geophys.* 97(2013) 3-10.
- 432 26. F.M. Fernandes, A. Fernandes, J. Pais, Assessment of the density and moisture content of asphalt
433 mixtures of road pavements, *Construction and Building Materials* 154(2017) 1216-1225.
- 434 27. A.K. Benson, Applications of ground penetrating radar in assessing some geological hazards: examples
435 of groundwater contamination, faults, cavities, *J. Appl. Geophys.* 33(1995) 177 – 193.
- 436 28. J.L. Davis, A.P. Annan, Ground-penetrating radar for high resolution mapping of soil and rock
437 stratigraphy, *Geophys. Prospect.* 37(1989) 531–551.

- 438 29. M. Tallini, A. Giamberardino, D. Ranalli, M. Scozzafava, GPR survey for investigation in building
439 foundations, in: *Ground Penetrating Radar, 2004. GPR 2004. Proceedings of the Tenth International*
440 *Conference on, IEEE, 2004, pp. 395-397.*
- 441 30. S. Malagodi, L. Orlando, S. Piro, E. Rosso, Location of Archaeological Structures Using GPR Method:
442 Three-Dimensional Data Acquisition, *Archaeological Prospection* 3(1996) 15-23.
- 443 31. M.H. Powers, G.R. Olhoeft, Modelling the GPR response of leaking, buried pipes, in: R.S. Bell, M.H.
444 Cramer (Eds.), *Symposium on the Application of Geophysics to Engineering and Environmental*
445 *Problems 1996, Society of Exploration Geophysicists, 1996, pp. 525-534.*
- 446 32. S. Lambot, E.C. Slob, I. van den Bosch, B. Stockbroeckx, M. Vanclooster, Modelling of ground-
447 penetrating radar for accurate characterization of subsurface electric properties, *IEEE Trans. Geosci.*
448 *Remote Sens.* 42.11(2004) pp. 2555–2568.
- 449 33. S. Lambot, I. van den Bosch, B. Stockbroeckx, P. Druyts, M. Vanclooster, E.C. Slob, Frequency
450 dependence of the soil electromagnetic properties derived from ground-penetrating radar signal
451 inversion, *Subsurface Sens. Technol. Appl.* 6(2005) 73–87.
- 452 34. J.A. Huisman, C. Sperl, W. Bouten, J.M. Verstraten, Soil water content measurements at different scales:
453 Accuracy of time domain reflectometry and ground-penetrating radar, *J. Hydrol.* 45(2001) 48–58.
- 454 35. S. Lambot, M. Javaux, F. Hupet, M. Vanclooster, A global multilevel coordinate search procedure for
455 estimating the unsaturated soil hydraulic properties, *Water Resour. Res.* 38.11(2002) 12-24.
- 456 36. S. Lambot, J. Rhebergen, I. van den Bosch, E.C. Slob, M. Vanclooster, Measuring the soil water content
457 profile of a sandy soil with off-ground monostatic ground penetrating radar, *VZI* 3(2004) 1063-1071.
- 458 37. L. Capozzoli, E. Rizzo, **Combined NDT techniques in civil engineering applications: Laboratory and real**
459 **test, *Construction and Building Materials*, 154(2017) 1139-1150.**
- 460 38. C. Maierhofer, S. Leipold, Radar investigation of masonry structures, *NDT&E Int.* 34(2001) 139–147.
- 461 39. L. Orlando, E.C. Slob, Using multicomponent GPR to monitor cracks in a historical building, *Journal of*
462 *Applied Geophysics* 67(2009) 327-334.
- 463 40. C. Patriarca, S. Lambot, M.R. Mahmoudzadeh, J. Minet, E.C. Slob, Reconstruction of sub-wavelength
464 fractures and physical properties of masonry media using full-waveform inversion of proximal
465 penetrating radar, *J. Appl. Geophys.* 74.1(2011) 26–37.
- 466 41. G. De Donno, L. Di Giambattista, L. Orlando, **High-resolution investigation of masonry samples through**
467 **GPR and electrical resistivity tomography, *Construction and Building Materials* 154(2017) 1234-1249.**
- 468 42. L. Binda, C. Colla, M.C. Forde, Identification of moisture capillarity in masonry using digital impulse
469 radar, *J Construct. Building. Mater.* 8.2(1994) 101–107.
- 470 43. L. Binda, G. Lensi, A. Saisi, NDE of masonry structures: use of radar tests for the characterization of
471 stone masonries, *NDT&E International*, 31.6(1998) 411-419.

- 472 44. F. Kurz, H. Sgarz, Measurement of Moisture Content in Building Materials using Radar Technology, in:
473 International Symposium Non-Destructive Testing in Civil Engineering (NDT-CE), Berlin, Germany, 2015.
- 474 45. S. Laurens, J.P. Balayssac, J. Rhazi, G. Klysz, G. Arliguie, Nondestructive evaluation of concrete moisture
475 by GPR: Experimental study and direct modeling, *Mater. Struct.* 38.9(2005) 827–832.
- 476 46. A. Kalogeropoulos, J. van der Kruk, J. Hugenschmidt, S. Busch, K. Merz, Chlorides and moisture
477 assessment in concrete by GPR full waveform inversion, *Near Surface Geophysics* 9.3(2011) 277–285.
- 478 47. R. Du Plooy, G. Villain, S.P. Lopes, A. Ihamouten, X. Dérobert, B. Thauvin, Electromagnetic non-
479 destructive evaluation techniques for the monitoring of water and chloride ingress into concrete: a
480 comparative study, *Materials and structures* 48.1-2(2015) 369-386.
- 481 48. S.F. Senin, R. Hamid, Ground penetrating radar wave attenuation models for estimation of moisture and
482 chloride content in concrete slab, *Construction and Building Materials* 106(2016) 659-669.
- 483 49. L. Binda, MD.E.1: determination of moisture distribution and level using radar in masonry built with
484 regular units, *Mater. Struct.* 38(2005) 283–288.
- 485 50. S. Lambot, M. Antoine, M. Vanclooster, E.C. Slob, Effect of soil roughness on the inversion of off-ground
486 monostatic GPR signal for non-invasive quantification of soil properties, *Water Resources Research*
487 42.3(2006). DOI: 10.1029/2005WR004416.
- 488 51. S. Lambot, E.C. Slob, I. van den Bosch, B. Stockbroeckx, B. Scheers, M. Vanclooster, Estimating soil
489 electric properties from monostatic ground-penetrating radar signal inversion in the frequency domain,
490 *Water Resources Res.* 40(2004).
- 491 52. C.T. Tai, *Dyadic Green Function in Electromagnetic Theory*, Piscataway, NJ, IEEE Press, 1994.
- 492 53. K. Michalski, J. Mosig, Multilayered media Green's functions in integral equation formulations, *IEEE*
493 *Trans. Antennas Propagat.* 45.3(1997) 508-519.
- 494 54. A.F. Peterson, S.L. Ray, R. Mittra, *Computational Methods for Electromagnetics*, New York, Oxford Univ.
495 Press, 1998.
- 496 55. E.C. Slob, J. Fokkema, Coupling effects of two electric dipoles on an interface, *Radio Sci.* 37.5(2002).
- 497 56. J. Hipp, Soil electromagnetic parameters as functions of frequency, soil density, and soil moisture, *Proc.*
498 *IEEE* 62.1(1974) 98-103.
- 499 57. M. Hallikainen, F. Ulaby, M. Dobson, M. El-Rayes, L. Wu, Microwave dielectric behaviour of wet soil, part
500 I: Empirical models and experimental observations, *IEEE Trans. Geosci. Remote Sens.* 1(1985) 25-34.
- 501 58. T. Heimovaara, E. de Winter, W. van Loon, D. Esveld, Frequency dependent dielectric permittivity from
502 0–1 GHz: Time domain reflectometry measurements compared with frequency domain network
503 analyser measurements, *Water Resources Res.* 32(1996) 3603–3610.
- 504 59. L. West, K. Handley, Y. Huang, M. Pokar, Radar frequency dielectric dispersion in sandstone: Implications
505 for determination of moisture and clay content, *Water Resources Res.* 39.2(2003) 1026.

- 506 60. V. Komarov, S. Wang, J. Tang, Permittivity and measurements, Encyclopedia of RF and microwave
507 engineering, 2005.
- 508 61. P. Hansen, N. Mladenović, J.A.M. Pérez, Variable neighbourhood search: methods and
509 applications, *Annals of Operations Research* 175.1(2010) 367-407.
- 510 62. L. Papa, I tuffi vulcanici nel costruito storico: Vulnerabilità e possibili trattamenti per la conservazione e il
511 restauro, Università degli Studi di Napoli Federico II, Napoli, Italy, 2011 (doctoral thesis).
- 512 63. L. Mollo, R. Greco, Moisture measurements in masonry materials by time domain Reflectometry, *J.*
513 *Mater. Civ. Eng.* 23.4(2010) 441-444.
- 514 64. M. El-Shenawee, E. Miller, Multiple-incidence/multi-frequency for profile reconstruction of random
515 rough surfaces using the three-dimensional electromagnetic fast multipole model, *IEEE Trans. Geosci.*
516 *Remote Sens.* 42.11(2004) 2499–2510.
- 517 65. A. Chanzy, A. Tarussov, A. Judge, F. Bonn, Soil water content determination using digital ground
518 penetrating radar, *Soil Sci. Soc. Am. J.* 60(1996) 1318– 1326.
- 519 66. L. Boithias, *Radio Wave Propagation*, McGraw-Hill, New York, 1987.
- 520 67. R. Agliata, L. Mollo, R. Greco, Use of TDR to compare rising damp in three tuff walls made with different
521 mortars, *J. Mater. Civ. Eng.* 29.4(2016) 04016262.
- 522 68. G.C. Topp, J. L. Davis, A.P. Annan, Electromagnetic determination of soil water content: Measurements
523 in coaxial transmission lines, *Water resources research* 16.3(1980) 574-582.